# Phase transitions and thermodynamic properties of yttria, $Y_2O_3$: Inelastic neutron scattering shell model and first-principles calculations

Preyoshi P. Bose,[1] M. K. Gupta,[1] R. Mittal,[1,*] S. Rols,[2] S. N. Achary,[3] A. K. Tyagi,[3] and S. L. Chaplot[1]

[1]*Solid State Physics Division, Bhabha Atomic Research Center, Trombay, Mumbai, 400085, India*

[2]*Institut Laue-Langevin, BP 156, 38042 Grenoble Cedex 9, France*

[3]*Chemistry Division, Bhabha Atomic Research Centre, Trombay, Mumbai, 400085, India*

(Received 25 May 2011; revised manuscript received 11 August 2011; published 12 September 2011)

Yttria ($Y_2O_3$) is a well-known ceramic material extensively used in industry. We report new neutron inelastic scattering measurement of the phonon density of states (PDOS) and lattice dynamic calculations using the *ab-initio* density functional theory and interatomic potential model, which are found to be in good agreement with each other. The model is then used in extensive free-energy calculation to understand the stability of various phases as a function of pressure and temperature. We find that one of the Y-O bonds shows a very large compression with increasing pressure, involving change of coordination around the Y atoms. This seems to provide the mechanism of the transition from the monoclinic phase to the hexagonal phase at the high pressure. We find that this transition is displacive in nature, and we also identify how the change of coordination affects the phonon spectra of the various phases.

DOI: 10.1103/PhysRevB.84.094301 PACS number(s): 78.70.Nx, 63.20.−e, 65.40.−b

## I. INTRODUCTION

Yttria ($Y_2O_3$) is chemically and structurally very close to the rare earths' oxides and hence falls in the category of rare-earth sesquioxides. It is an industrially and technologically very useful ceramic material that is used to increase the ductility of aluminum oxide (alumina ceramics)[1] and also to stabilize the cubic and tetragonal phases of zirconia, which is particularly important in the design of solid oxide fuel cells. Among the many different uses of Yttria, one can also mention that its dense polycrystalline form has been used in nuclear applications[2] and its nanoparticles in biomedical field.[3] Another important aspect of ceramic materials concerns the continuous laser action that has been obtained in crystals such as $Er_2O_3$, $Yb_2O_3$, and $Y_2O_3$.[4] These compounds exhibit three structural polymorphisms: cubic, monoclinic, and hexagonal, commonly known as C-, B-, and A-type structures, respectively.[5] The Cubic[6,7] form of $Y_2O_3$ being stable at room temperature and ambient pressure. The structural stability of yttria with pressure and temperature makes it useful in many industrial applications. The study of its thermodynamic properties and phase transition is therefore of great importance and is the subject of the current paper.

Many attempts have been made to understand the structural stability of yttria under high pressure and temperature. The evidence of its high pressure phase transition from cubic to monoclinic phase was first reported[8] at 2.5 GPa and 1273 K. Later the reversible nature of the transition and enhanced stability of the monoclinic phase under higher pressure and temperature have been reported,[9] while the hexagonal phase was proposed to be the next favorable stable high pressure phase. Single crystals of the monoclinic phase of $Y_2O_3$ were synthesized[10] from high pressure experiments carried out on a sample in the cubic phase. The Raman[11] spectroscopy measurements on these yttria single crystals reported two phase transitions, viz. cubic to monoclinic and monoclinic to hexagonal at 12 and 19 GPa, respectively. Recent[12] high pressure x-ray diffraction experiments on cubic $Y_2O_3$ at room temperature showed coexistence of the cubic, monoclinic, and hexagonal phases in a pressure range from 15 GPa to 25.6 GPa. On further compression the sample completely transformed to the hexagonal phase at 25.6 GPa. The cubic phase of $Sc_2O_3$ was reported to remain stable[12] up to 30 GPa at room temperature, whereas a transition to a $Gd_2S_3$ (*Pnma*, $Z = 4$) type phase was observed at much lower pressure (at 18 GPa) and higher temperatures. Another specific aspect stands in the kinetics that seems to play a major role in determining the sequence of phase transitions for yttria. As well, synchrotron x-ray diffraction measurements show that Eu-doped $Y_2O_3$ exhibit a cubic-monoclinic-hexagonal sequence of phase transitions[13] under pressure at ambient temperature, while pure cubic $Y_2O_3$ shows a direct transition to hexagonal phase under these conditions. The changes that occurred in the lattice vibrations and electronic states of $Y_2O_3$ by Eu doping seem to be responsible for these differences. Shock studies[14] have been reported on $Y_2O_3$ that indicate phase transition to the monoclinic structure over a pressure range of 12 to 20 GPa.

The measurements of the elastic moduli of yttria from 300–1473 K have been reported by James *et al.*[15] Yttria is found to be stable up to about 2705 K. The cubic phase transforms[16] to the hexagonal phase at 2512 K just before melting. The phase is also identified as the disordered cubic fluorite phase. The stability of the crystalline phases of $Y_2O_3$ at high pressures has also been studied by calculating[12] enthalpy in various phases using the *ab-initio* method. A molecular dynamic study[17] using a Pauling-type pair potential was carried out to study the melting process of yttria, but the authors failed at reproducing the correct melting temperature. Later, another Buckingham potential was used to study[18] the structure and melting of $Y_2O_3$. *Ab-initio* molecular dynamics[18] study of the structure of crystalline yttria ($Y_2O_3$) up to 5000 K indicated melting at 3150 K.

Recent experimental investigations[11] performed on good quality single crystals of rare-earth oxides have brought considerable insights into the thermodynamical properties. The assignment of the Raman spectra for the cubic phase of yttria was proposed[19] on the basis of a valence force model

 

consisting of 20 adjustable parameters. We have carried out extensive lattice dynamical studies to provide insight into the phase transition mechanism of yttria. The phonon spectrum has been calculated using the shell model as well as *ab-initio* approach. We have also performed inelastic neutron scattering investigations to derive the phonon density of states (PDOS) of CUBIC $y_2O_3$ ceramics at ambient pressure and temperature. The shell-model calculations results are in good agreement with the inelastic neutron data and *ab-initio* calculations. This allowed testing of our model, which is used to explore the high pressure and high temperature part of the phase diagram. Further the model has been used for calculation of free energy in various phases of $Y_2O_3$. Our approach allows us to calculate the pressure dependence of the vibrational energy contribution to the Gibbs free energy, as discussed in Sec. VB, which may be computationally expensive to calculate using *ab-initio* approach as cubic and monoclinic phase of $Y_2O_3$ has 40 and 30 atoms/primitive cell. We have calculated thermodynamic properties and found a fair agreement with various available experimental data.

Our paper is organized as follows. In Sec. II we discuss the structure of yttria in the different phases, while Secs. III and IV provide details on the inelastic neutron scattering investigations and the model calculations, respectively. The discussion of the results is organized in four parts in Sec. V: part VA deals with the lattice dynamics, VB treats essentially the free-energy calculations of the phase diagram, VC the thermodynamics observables, and VD the mean-squared amplitudes of atoms in various phases of yttria.

## II. STRUCTURE

The cubic structure of yttria crystallizes in the space group $Ia3$ (Fig. 1). The body-centered cubic structure has eight formula units/primitive cell. The structure has two types of yttrium atoms, Y1 and Y2, occupying $8b$ ($\frac{1}{4}$, $\frac{1}{4}$, $\frac{1}{4}$) and $24d$ ($x$, 0, $\frac{1}{4}$) crystallographic positions with the oxygen atoms placed at 48e ($x$, $y$, $z$). The structure consists of $Y1O_6$ and $Y2O_6$ polyhedral units. The application of pressure on the cubic cell changes the structure (Fig. 1) to a monoclinic cell (space group is $C2/m$) with six formula units/primitive cell. In this particular structure there are three types of yttrium atoms, Y1, Y2, Y3, and five different types of oxygen atoms, namely, O1, O2, O3, O4, and O5. All the atoms in the monoclinic cell are placed at $4i$ ($x$, 0, $z$) positions except for O5 which is at $2b$ (0, 0.5, 0) site. The monoclinic phase further transforms to the hexagonal phase with increasing pressure. The hexagonal primitive cell (space group $P\bar{3}m1$) has only one formula unit. The yttrium atoms and the O2-type oxygen atom in the hexagonal phase are placed at $2d$ (1/3, 2/3, $z$), while O1 oxygen atoms occupy $1a$ (0, 0, 0).

## III. EXPERIMENTAL

The polycrystalline sample in the cubic phase of $Y_2O_3$ was characterized using x-ray diffraction. The analysis of powder diffraction data indicated that the sample is in single phase. The inelastic neutron scattering experiments were performed using the thermal time-of-flight neutron spectrometer IN4 at the Institute Laue Langevin (ILL) located in Grenoble (France). A quantity of 25 grams of polycrystalline $Y_2O_3$ sample was placed inside a thin aluminum sample holder. The incident neutron wavelength of 2.4 Å (14.2 meV) was chosen, which allowed the spectra to be obtained in the neutron energy gain mode at 300 K. We used a Fermi chopper speed of 28 000 RPM to allow for a time focusing condition in the inelastic regime (inelastic-time focusing). The detector bank of IN4 covers scattering angles up to 120°. After usual correction (see, for example, Ref. 20), the spectra at all detector angles were summed up to increase the statistics and to average out the coherent effect which is necessary to allow for a correct estimation of the PDOS (the so-called "incoherent approximation"). In the final stage the dynamical structure factor $S(Q, E)$ is obtained, from which the neutron weighted "generalized" PDOS $g^{(n)}(E)$ can be extracted using the following expression[21]:

$$g^{(n)}(E) = A\left\langle \frac{e^{2W_k(Q)}}{Q^2}\frac{E}{n(E,T)}S(Q,E)\right\rangle,$$

where $E$ is the energy transfer from the sample to the neutron $n(E,T) = [\exp(E/k_BT) - 1]^{-1}$, $A$ is the normalization constant, and the quantity within $\langle\text{—}\rangle$ represents the proper average over all $Q$ values at a given energy. $2W(Q)$ is the Debye-Waller factor.

The neutron-weighted PDOS writes,

$$g^n(E) = B\sum_k \left\{\frac{4\pi b_k^2}{m_k}\right\} g_k(E),$$

where $B$ is the normalization constant and $\sigma_k$, $m_k$, and $g_k(E)$ are total neutron scattering cross section, mass, and partial density of states of the $k$th atom in the unit cell, respectively. The values of the scattering cross section can be found from Ref. 21. The weighting factors $\frac{4\pi b_k^2}{m_k}$ for various atoms in the units of barns/amu are $Y = 0.086$ and $O = 0.265$ barns/amu, which imply that the main contribution of the signal originates from oxygen modes (75%).

## IV. LATTICE DYNAMICAL CALCULATIONS

Lattice dynamical calculations require information about the interatomic forces that can be obtained either by using a quantum-mechanical *ab-initio* formulation or by using semi-empirical interatomic potentials. We have performed calculations using both the methods. The pseudopotential generated by PBE exchange correlation functional[22] under generalized gradient approximation (PBE-GGA) has been used for *ab-initio* calculations in cubic phase of $Y_2O_3$. The calculations have been carried out using plane-wave basis sets and Quantum Espresso software package.[23] We have chosen $4 \times 4 \times 4$ k-mesh for self-consistent field calculations with energy cutoff of 45 Rydberg, which is found to be sufficient for convergence of the order of meV. The k-point mesh has been generated using the Monkhorst-pack method.[24] Dynamical matrices were calculated on a $3 \times 3 \times 3$ mesh in the irreducible Brillouin zone.

The shell model is based on a transferable potential that consists of long-range Coulmbic interaction, short-range Born-Mayer type repulsive terms, and weakly attractive van der

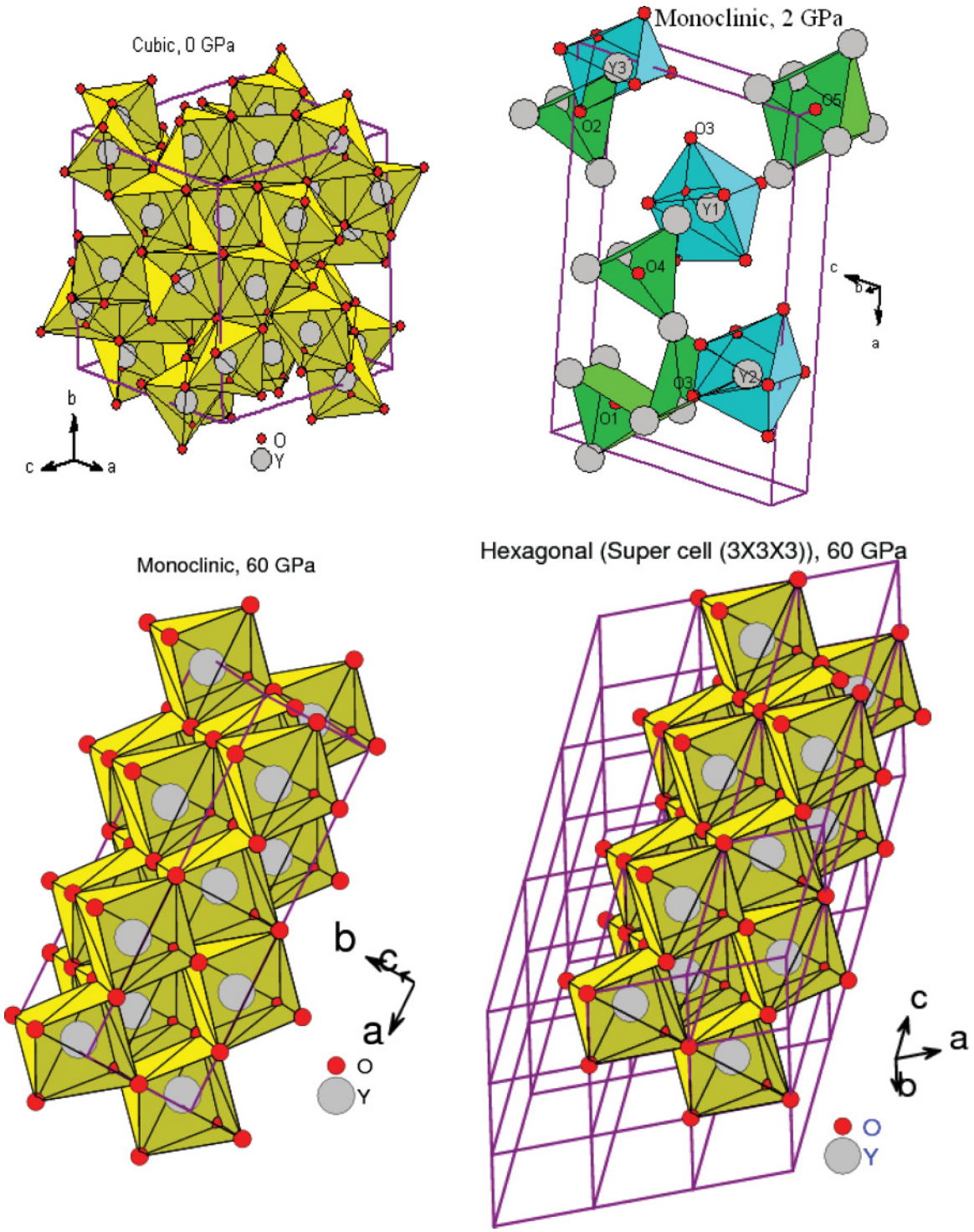


FIG. 1. (Color online) Polyhedral representation of the cubic (space group *Ia3*), monoclinic (*C2/m*), and hexagonal ($P\bar{3}m1$) phases of $Y_2O_3$.

Waals terms. The form of the interatomic potential used in our model is given by the following expression,

$$V(r) = \frac{e^2}{4\pi\varepsilon_0}\frac{Z(k)Z(k')}{r} + a\exp\left(\frac{-br}{R(k)+R(k')}\right) - \frac{C}{r^6},$$

where, $a = 1822$ eV and $b = 12.364$ are empirical constants. We have successfully used[25,26] this set of parameters in the lattice dynamical calculations of several complex solids. The term $C = 100$ eVÅ$^6$ accounts for the van der Waals interaction between O-O pairs. The effective charge $Z(k)$ and radii $R(k)$ parameters used in our calculations are $Z(Y) = 2.4$, $Z(O) = -1.6$, $R(Y) = 1.931$ Å, and $R(O) = 1.89$ Å. The polarizability of the oxygen atoms is introduced in the framework of the shell model.[27,28] The shell charge and

TABLE I. Comparison between the calculated (0 K) and experimental (300 K) structural parameters of $Y_2O_3$. The structural parameters for the cubic phase calculated using the *ab-initio* approach are given in parentheses. For cubic phase (space group *Ia*3) the Y1, Y2, and O atoms are located at 8*b* ($\frac{1}{4}$, $\frac{1}{4}$, $\frac{1}{4}$) and 24*d* ($x$, 0, $\frac{1}{4}$), and 48e ($x$, $y$, $z$), respectively. For monoclinic structure (space group $C2/m$) there are three types of yttrium atoms, Y1, Y2, Y3, and five different types of oxygen atoms namely, O1, O2, O3, O4, and O5. All the atoms in the monoclinic cell are placed at 4*i* ($x$, 0, $z$) position except for O5, which is at 2*b* (0, 0.5, 0) site. In the hexagonal structure (space group $P\bar{3}m1$) the Y, O1, and O2 atoms are located at 2*d* (1/3, 2/3, $z$), 1*a* (0, 0, 0) and 2*d* (1/3, 2/3, $z$), respectively.

| Cubic | Present calculation (0 GPa, 0 K) | | | Experimental data (0 GPa, 300 K)[6,7] | | |
|---|---|---|---|---|---|---|
| $a$(Å) | 10.61 (10.63) | | | 10.604 | | |
| V/primitive cell (Å$^3$) | 597.2 (600) | | | 596.18 | | |
| | $x$ | $y$ | $z$ | $x$ | $y$ | $z$ |
| Y(1) | 0.250 | 0.250 | 0.250 | 0.2500 | 0.2500 | 0.2500 |
| Y(2) | −0.033(−0.033) | 0.000 | 0.250 | −0.0290 | 0.0000 | 0.2500 |
| O | 0.389(0.391) | 0.154(0.152) | 0.378(0.380) | 0.3910 | 0.1540 | 0.3804 |
| Monoclinic | Present calculation (15 GPa, 0 K) | | | Experimental data (12 GPa, 300 K)[10] | | |
| $a$(Å) | 13.54 | | | 13.871 | | |
| $b$(Å) | 3.41 | | | 3.449 | | |
| $c$(Å) | 8.43 | | | 8.586 | | |
| $\beta$ | 99.7 | | | 100.12 | | |
| V (Å$^3$) | 383.3 | | | 404.37 | | |
| | $x$ | $y$ | $z$ | $x$ | $y$ | $z$ |
| Y(1) | 0.635 | 0 | 0.490 | 0.6352 | 0 | 0.4885 |
| Y(2) | 0.692 | 0 | 0.141 | 0.6896 | 0 | 0.1364 |
| Y(3) | 0.966 | 0 | 0.184 | 0.9667 | 0 | 0.1864 |
| O(1) | 0.127 | 0 | 0.284 | 0.1240 | 0 | 0.2810 |
| O(2) | 0.829 | 0 | 0.028 | 0.8230 | 0 | 0.0310 |
| O(3) | 0.794 | 0 | 0.374 | 0.7900 | 0 | 0.3780 |
| O(4) | 0.472 | 0 | 0.340 | 0.4720 | 0 | 0.3440 |
| O(5) | 0 | 0.5 | 0 | 0 | 0.5 | 0 |
| Hexagonal | Present calculation (48 GPa, 0 K) | | | Experimental data (0 GPa, 2570 K)[30] | | |
| $a$(Å) | 3.58 | | | 3.810 | | |
| $c$(Å) | 5.41 | | | 6.080 | | |
| $V$(Å$^3$) | 60.0 | | | 76.43 | | |
| | $x$ | $y$ | $z$ | | | |
| Y | 0. 333 | 0. 667 | 0.242 | | | |
| O1 | 0.000 | 0.000 | 0.000 | | | |
| O2 | 0. 333 | 0. 667 | 0.667 | | | |

shell-core force constants for oxygen atoms are −3.75 and 170 eV/Å$^2$, respectively. The crystal structure parameters were obtained by minimizing the free energy at $T = 0$ K. We find that the calculated structure is close to that obtained using diffraction experiments. The interatomic potential model also satisfies the dynamic equilibrium condition of the lattice, i.e., the phonon frequencies have real values for all the wave vectors in the Brillouin zone for the calculated structure. We have used a mesh of 10 × 10 × 10 k-points for the calculation of the PDOS and for the thermal expansion in the cubic phase. The parameters of the potential were fitted to reproduce various other available experimental data, namely the structure, the elastic constants, etc. The good agreement between the calculated and experimental structure (Table I) and other dynamical properties indicate that our model is quite satisfactory. The potential is then extended for the calculations in the high-pressure monoclinic and hexagonal phases. The calculations are carried out using the software DISPR[29] developed at Trombay.

## V. RESULTS AND DISCUSSION

### A. Structure and PDOS

The calculated structures (Table I) in the cubic and monoclinic phases agree very well with the experimental data. Yttria is known to transform[11,12] to the hexagonal phase at high pressures. The structure of the hexagonal phase at high pressure has not been refined yet, but x-ray measurements performed at 2570 K enabled the lattice parameters of $Y_2O_3$ to be measured[30] in the hexagonal phase. $Nd_2O_3$ is iso-structural to $Y_2O_3$ and is known to crystallize in the hexagonal structure[31] at ambient pressure. To proceed with the calculation in the hexagonal phase of $Y_2O_3$, we have taken the atomic coordinates of $Nd_2O_3$ in the hexagonal phase and have minimized the structure with the potential parameters of $Y_2O_3$. We find that the hexagonal phase of yttria is stable only above 26 GPa. The calculated lattice parameters in the hexagonal phase at 48 GPa and 0 K are compared with the experimental data[30] obtained at 2570 K at 0 GPa in Table I. We find that the calculations compare satisfactorily (Table I)

TABLE II. Comparison between the calculated and experimental[15] elastic constants and bulk modulus in the cubic phase of $Y_2O_3$ at $T = 0$ K and ambient pressure (in GPa units).

| | | Calculated | |
|---|---|---|---|
| | Experimental[15] | Potential Model | *ab-initio* |
| C11 | 223.7 | 206 | 233 |
| C12 | 112.4 | 103 | 139 |
| C44 | 74.6 | 59 | 72 |
| B | 156 | 138 | 170 |

with the experimental structure at high temperatures. The calculated elastic properties of the cubic phase agree fairly well with available experimental data[15] (see Table II). The calculations indicated stability of the monoclinic and hexagonal phases above 15 and 48 GPa, respectively (as discussed subsequently in Sec. VB). The bulk modulus values have been calculated at these pressures. The calculated values are 207 and 292 GPa for monoclinic and hexagonal phases, respectively.

The comparison between the experimental and calculated neutron-weighted PDOS of yttria in the cubic phase using the potential model as well as *ab-initio* approach is shown in Fig. 2. The experimental spectrum can be divided into two parts: the low-frequency part (below 40 meV) consists of a series of weak features (14, 17, and 20 meV) superimposed to a general curve having a maximum at 20 meV; the high frequency part features intense contributions at 45 meV (a multicomponent peak), 60 meV, and 72 meV. No modes are observed for

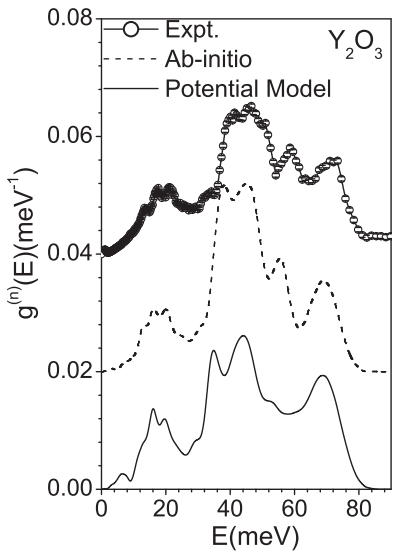


FIG. 2. The comparison of the calculated and experimental neutron-weighted PDOS for cubic phase of yttria at ambient pressure. The *ab-initio* as well as potential model calculations in the cubic phase are carried out at 0 K, while the measurements were performed at 300 K. For better visibility the experimental and calculated phonon spectra using *ab-initio* approach are shifted along the *y*-axis by 0.04 $meV^{-1}$ and 0.02 $meV^{-1}$, respectively. The multiphonon contribution calculated using the Sjolander formalism[38] has been subtracted from the experimental data. The calculated spectra have been convoluted with a Gaussian of FWHM of 10% of the energy transfer in order to describe the effect of energy resolution in the experiment.

frequencies higher than 80 meV. The general characteristics of the experimental features are well reproduced by the calculations. Both the calculations agree very well with the experimental data. In particular the calculations reproduce very well the low-frequency part of the spectrum where the modes involving mainly Y vibrations dominate the dynamics, as indicated by the partial density of states (see Fig. 3). The comparison of calculated partial density of states (Fig. 3) of various atoms in cubic $Y_2O_3$ from both the potential as well as *ab-initio* calculations indicates slight difference in the phonon spectra for oxygen atoms above 40 meV.

Our calculations performed on the monoclinic phase indicate that the phonon modes in this phase are stable only for pressure above 15 GPa. The transition from the cubic to the monoclinic phase (as discussed subsequently in Sec. VB) involves a 5.7% drop in unit cell volume and a change of the coordination of the Y atoms. In the cubic phase all the Y atoms have six-fold coordination with their oxygen neighbors, while in the monoclinic unit cell, Y atoms form $YO_6$ and $YO_7$ polyhedral units in the ratio of 1:2. The calculated density of states, at 15 GPa, of the cubic and the monoclinic phases are presented in Fig. 3, together with that in the cubic phase at 0 GPa. If the volume reduction from 0 GPa to 15 GPa in the cubic phase is reflected by an overall hardening of the phonon modes, the unit cell contraction between the monoclinic and the cubic cell at 15 GPa only results in a general smoothing of the structure of the cubic DOS, which is typical of symmetry reduction, without clear transfer of DOS weight in the investigated frequency range.

In Fig. 3 we compare the phonon modes in the monoclinic and hexagonal phases at 48 GPa. Our calculations show that the phonon modes in the hexagonal phase are stable from a pressure of 26 GPa. The monoclinic to hexagonal transition (as discussed subsequently in Sec. VB) involves a volume drop of only 1%, and all the Y atoms form $YO_7$ polyhedra in the hexagonal phase. Due to their large mass, Y atoms in both phases mainly contribute at low energies up to 45 meV, while the oxygen atoms contribute in the whole energy range. The most important difference between the spectra is observed in the oxygen spectrum where a double peak structure located at 45 meV in the monoclinic is up-shifted by 10 meV in the hexagonal phase. The rather small changes in the phonon spectra suggest that both phases are rather similar as far as dynamics is concerned.

The phonon dispersion has been calculated (Fig. 4) along the high symmetry directions in the cubic phase using potential model as well as *ab-initio* method. In general the calculated nature of dispersion relation is nearly the same from both the methods, as also reflected in the calculated density of states (Figs. 2 and 3). We note that the transverse acoustic modes near the zone boundary along (110) (Fig. 4) are less dispersive in model potential calculations than in the *ab-initio* calculations. This smaller dispersion results in a peak in the density of states calculations (Figs. 2 and 3) from model potential at 7 meV. These vibrations mainly involve Y atoms (Fig. 3).

### B. Free energy and phase diagram

As shown previously, the calculated phonon spectra from the model as well as *ab-initio* calculations agree very well with

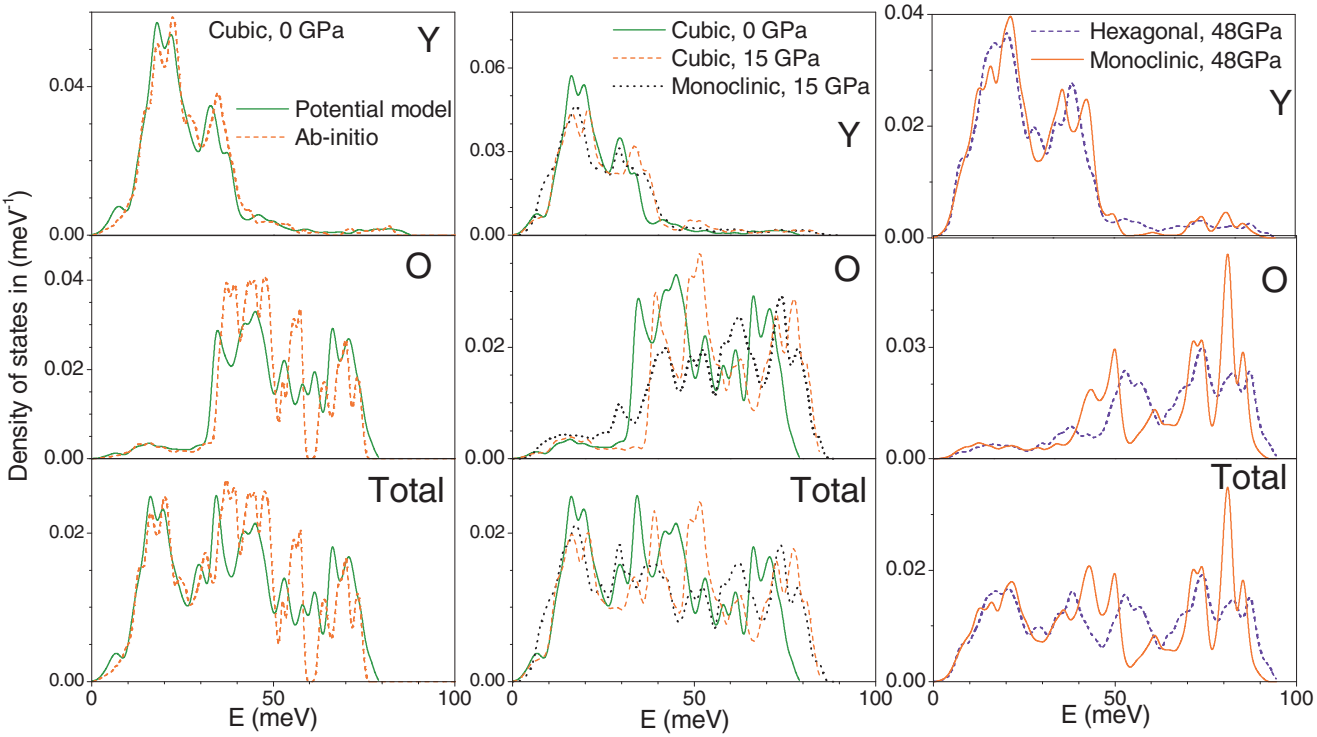


FIG. 3. (Color online) The calculated partial densities of states in various phases of $Y_2O_3$. The calculations in the cubic phase at 0 GPa are carried out using both the *ab-initio* and potential model, while at high pressure the calculations in various phases are performed only using the potential model.

the experimental data, indicating that the potential model can be used to obtain the phase diagram of yttria. The Gibbs free energy was calculated using the model potential in the various phases of $Y_2O_3$. The Gibbs free energy of the $n^{\text{th}}$ phase is given by

$$G_n = \phi_n + PV_n - TS_n,$$

where, $\phi_n$, $V_n$, and $S_n$ respectively relate to internal energy, lattice volume, and vibrational entropy of the $n^{\text{th}}$ phase. The Gibbs free energy of the various phases of $Y_2O_3$ are then compared at different pressures for a fixed temperature, which allows deriving the phase diagram presented in Fig. 5. We find that above 15 GPa at 300 K the monoclinic phase has lower free energy as compared to the cubic phase, and the phonon modes are stable. The calculations therefore predict the transition from cubic to monoclinic phase at this critical pressure, while experimental data[11] report this transition at 12 GPa at room temperature.

The difference between the free energies of the competing monoclinic and hexagonal phases of $Y_2O_3$ as a function of pressure (at 300 K) is reported in Fig. 6. The calculations show that the transition from the monoclinic to the hexagonal phase at 48 GPa (Fig. 5) is of first order in nature, as can be seen from the nonzero slope of the free-energy difference (Fig. 6) between the two phases at the transition pressure. The experimental data[12] show that the hexagonal phase is stable at pressures above a critical pressure of 25.6 GPa. The Gibbs free-energy calculation qualitatively reproduces the phase diagram of yttria. This is highly satisfactory since usually it is very difficult to reproduce free-energy differences with requisite high accuracy for phase diagram calculation. It is also a very difficult task to identify equilibrium phases from experiments at high pressure due to large hysteresis. The critical pressure for phase transition is also affected by the kinetics and also depends on the doping[13] of rare-earth ions in $Y_2O_3$. Such effects are not accounted for in our investigations.

The calculated equations of state of the monoclinic and hexagonal structures overlap above 62 GPa, as discussed in Sec. VC. This is reflected in the vanishing value of the free-energy difference (Fig. 6) between the two phases above this pressure. The calculated atomic coordinates and unit cell parameters at 62 GPa used for plotting the structure in the monoclinic and hexagonal phases [Fig. 1(c), 1(d)] show that both structures are actually identical. In other words we can find a hexagonal cell inside the monoclinic cell beyond 62 GPa. We have also tried to sketch a hexagonal unit cell (Fig. 7) inside the larger monoclinic cell at 48 GPa. As expected, the cell we could find is not perfectly hexagonal, but the figure shows the relationship between the two structures and the way the atoms have to move during the phase transition. This indicates that the transition from monoclinic to hexagonal phase involves small atomic displacements.

Recently, density functional theory calculations[12] for $Y_2O_3$ have been carried out in the local density approximation (LDA) and GGA approximations. The stability of the various phases at high pressures was determined by calculating the enthalpy differences between the cubic, monoclinic, and hexagonal phases. These calculations show that the cubic to monoclinic phase transition occurs at 2 GPa and 7 GPa using LDA and GGA, respectively, while the transition from the monoclinic to

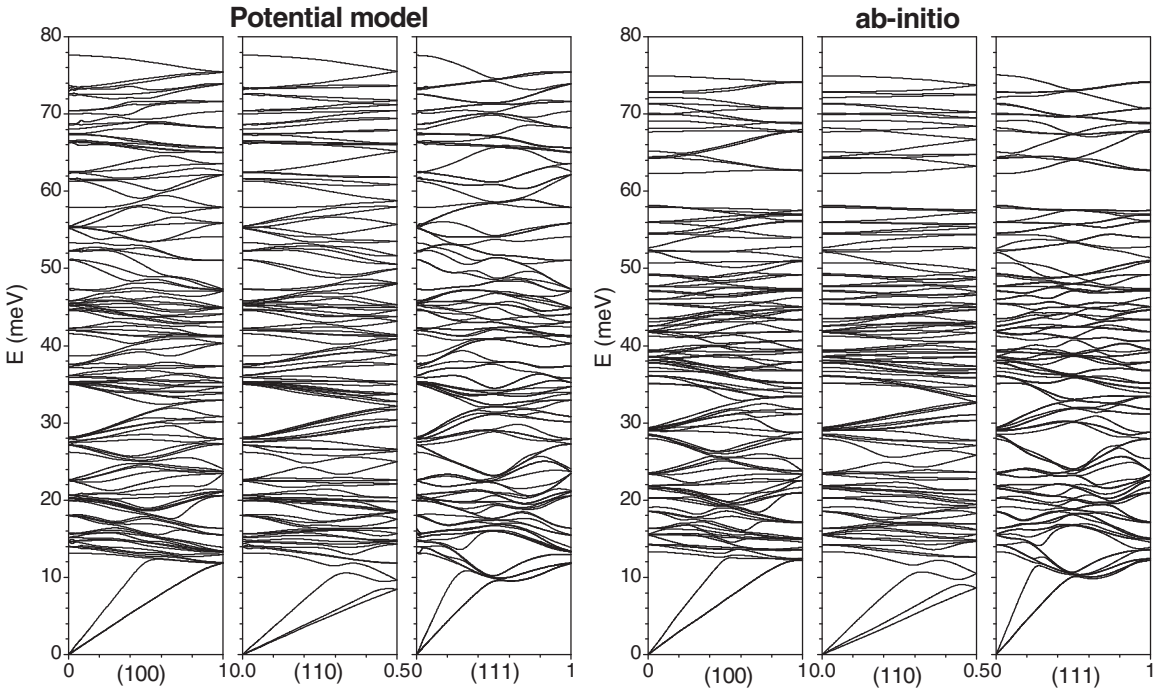


FIG. 4. Phonon dispersions for the cubic phase of $Y_2O_3$ as obtained using both the *ab-initio* and potential model.

the hexagonal phase is estimated at 9.5 GPa (LDA) and 20 GPa (GGA), respectively. The monoclinic to hexagonal transition is found to be displacive in nature, which is also consistent with our calculations.

We observe from our calculations that the difference between the free energies of the monoclinic and of the hexagonal phases in the pressure range of 26–62 GPa (Fig. 6) is very small. As shown in Fig. 6 the difference becomes zero above 62 GPa, suggesting the presence of a second-order transition between the two phases. The small difference in free energy can be tuned by the incorporation of a small amount of impurity ion in the $Y_2O_3$ lattice. This might be the origin of the coexistence of the monoclinic and hexagonal phases at high pressure[12] or for the two different sequences of phase transition[13] for pure $Y_2O_3$ (cubic- hexagonal) and Eu-doped $Y_2O_3$ (cubic-monoclinic-hexagonal) with temperature. As already discussed in the introduction, the cubic phase of yttria transforms to the hexagonal phase[30] at about 2512 K, before melting (at 2705 K). However, our calculations carried out at 0 K show that the hexagonal phase has stable phonon modes only above 26 GPa. Due to the extreme anharmonicity of the phonons close to the melting temperature, the hexagonal phase might be stabilized[30] before melting of $Y_2O_3$ at 2705 K.

### C. Thermodynamic properties

We have used the PDOS calculated in the different phases to further derive thermodynamic properties like the specific heat, thermal expansion, and the equation of state. The specific heat calculated in the cubic phase is compared with the experimental data obtained from various sources[32–35] and is shown in Fig. 8. Our calculations are close to the data given in the JANAF table.[36] The calculation of the thermal expansion is carried out in the quasiharmonic approximation for which each

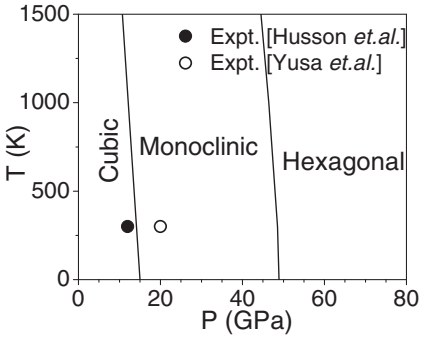


FIG. 5. The calculated phase diagram obtained from free-energy calculations. The closed and open circles are the experimental data for the cubic to monoclinic[11] and monoclinic to hexagonal[12] phase transitions, respectively.

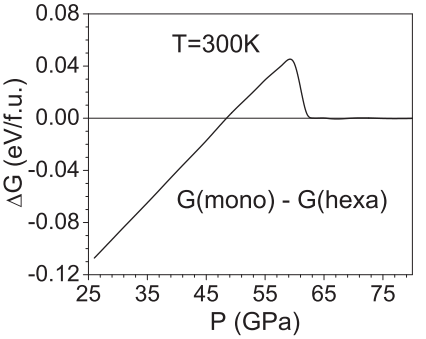


FIG. 6. The difference in the free energies of hexagonal and monoclinic phases of $Y_2O_3$ as a function of pressure at 300 K.

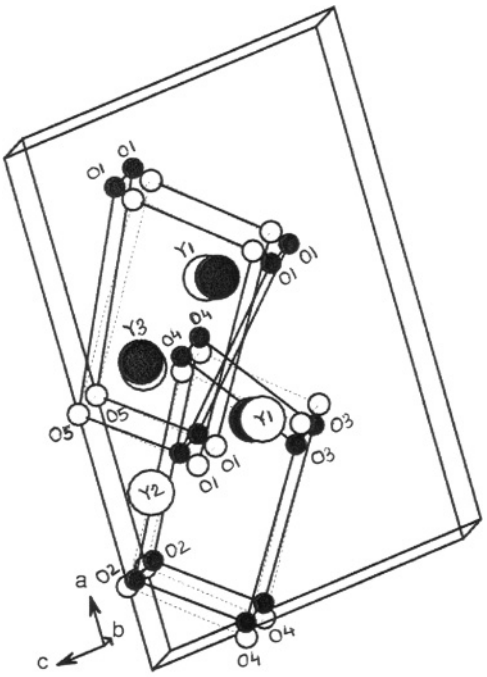


FIG. 7. The relationship between the monoclinic and hexagonal structures. The larger cell and the labeling of the axes correspond to the monoclinic structure. In this monoclinic cell we are able to draw a distorted hexagonal cell (solid line) at 48 GPa. We have also depicted the hexagonal unit cell (dashed line) corresponding to the transformed structure at 48 GPa. The solid and open symbols correspond to the atomic positions in the monoclinic and hexagonal cells respectively at 48 GPa. The labeling of atoms is as per the monoclinic unit cell shown in Fig. 1.

phonon mode contributes to the volume thermal expansion coefficient[27] given by

$$\alpha_V = \frac{1}{BV}\sum_i \Gamma_i C_{Vi}(T),$$

where $\Gamma_i (= -\partial ln E_i/\partial ln V)$ and $C_{vi}$ are the mode Grüneisen parameter and specific heat of the $i$th vibrational state of the crystal. The calculation of thermal expansion requires contribution from all the phonons in the Brillouin zone. As already mentioned in Sec. IV, we have used a mesh of $10 \times 10 \times 10$ k-points for the calculation of the phonon spectra in the cubic phase. The calculated volume dependence

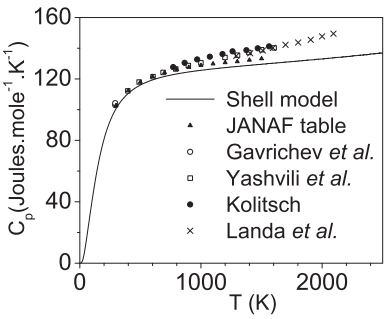


FIG. 8. The calculated and experimental[32–36] specific heat for cubic yttria at $P = 0$.

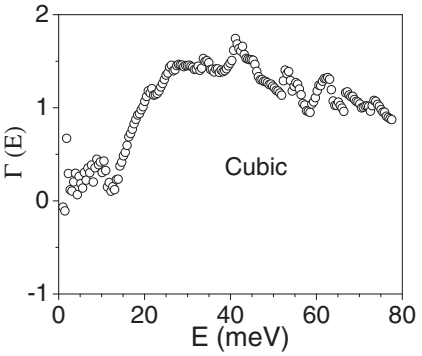


FIG. 9. The calculated Grüneisen parameter as a function of energy in the cubic phase of yttria.

of phonon frequencies has been used for the calculation of Grüneisen parameter $\Gamma(E)$ (Fig. 9), which is averaged for all phonons of energy $E$ in the Brillouin zone. $\Gamma(E)$ values lie between $-0.5$ to 1.8 and show considerable variation with energy. The comparison between the calculated and experimental thermal expansion in the cubic phase of yttria is shown in Fig. 10. Our procedure for the calculation of this important quantity is applicable only when explicit contributions to the total anharmonicity attributable to large thermal amplitude of atom displacements is not very significant. In our calculations the contribution to the thermal expansion is essentially from the implicit anharmonicity, i.e., accounted from the dependence of the phonon frequencies with the volume. The melting temperature[37] of $Y_2O_3$ is 2705 K, and the experimental thermal expansion data[16] are available up to about 2540 K. We find that our calculations are in very good agreement with the experimental thermal expansion up to 2200 K, a temperature above which a deviation from linear dependence with the volume is observed.

The calculated equation of state for the cubic, monoclinic, and hexagonal phases of yttria is shown in Fig. 11. The crystal structures at high pressures are obtained by minimization of the Gibb's free energy with respect to the structural variables keeping the space group unchanged. Our calculations show that a drop of about 5.7% in volume accompanies the cubic to monoclinic phase transition at 15 GPa, while during the transition to the hexagonal phase at 48 GPa there is a reduction of unit cell volume of about 1%. We have calculated structures in both the monoclinic and hexagonal space groups up to 80 GPa. We find that above 62 GPa, all the Y atoms have 7-fold

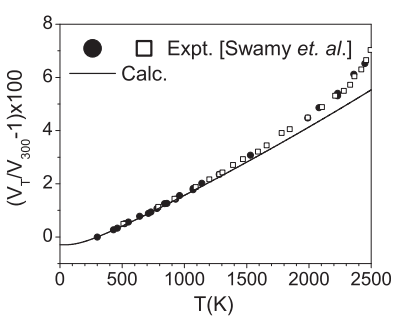


FIG. 10. The calculated and experimental[16] thermal expansion behavior of cubic yttria.

coordination, as found in the hexagonal phase (Fig. 1). Above 62 GPa, the variation of volume with increasing pressure (see Fig. 11) is calculated to be the same in both space groups.

### D. Mean-squared amplitudes of atoms in various phases of yttria

In order to understand the nature of the phonon modes in the various phases, we have plotted the contribution of each phonon mode to the mean-squared amplitudes $\langle u^2 \rangle$ (Fig. 12) of atoms in the various phases of $Y_2O_3$. In the cubic phase at 15 GPa, modes up to 8 meV involve the same displacements of all atoms, indicating that these modes are largely acoustic. From 8–17 meV the phonon modes correspond to simultaneous translations and rotations of $YO_6$ octahedral units. The modes from 17 to 35 meV involve

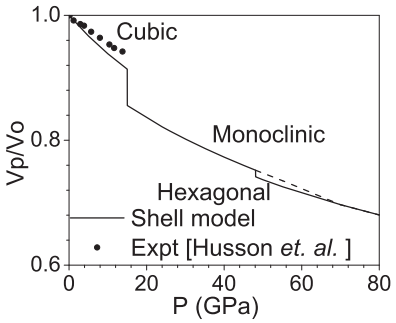


FIG. 11. The calculated and experimental[11] equation of state for in-various phases of $Y_2O_3$ at $T = 0$. $V_0$ and $V_P$ refer to the values at ambient pressure and pressure $P$, respectively. In order to indicate that the monoclinic structure smoothly approaches the hexagonal structure at 62 GPa, the calculations in the monoclinic phase are shown up to 80 GPa.

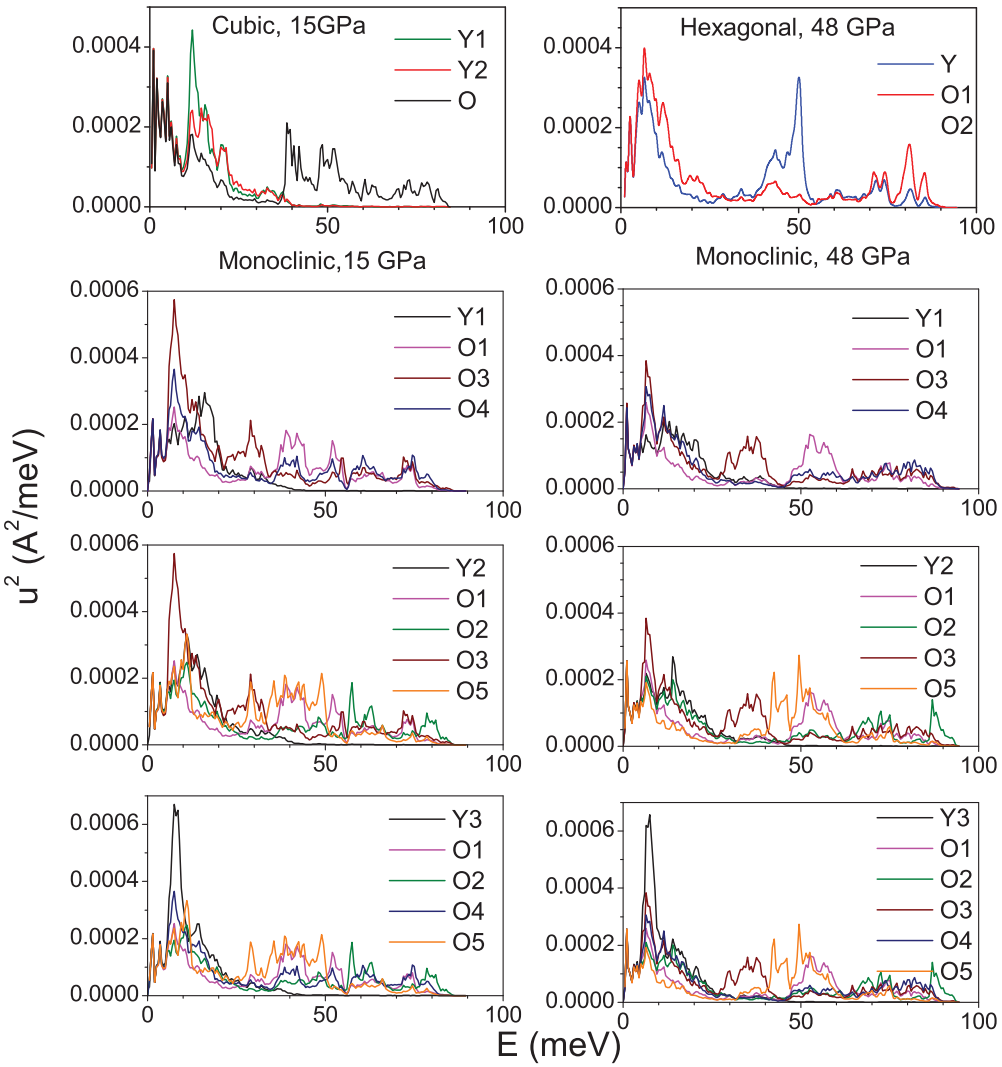


FIG. 12. (Color online) The calculated contribution to the mean-squared amplitude of various atoms arising from phonons of energy $E$ (integrated over the Brillouin zone) at $T = 300$ K in various phases of $Y_2O_3$. The cubic phase has six coordinated polyhedral units around Y1 (Y1, 6O) and Y2 (Y2, 6O) atoms. The asymmetric unit cell of monoclinic phase consists of three Y (Y1, Y2, Y3) atoms and five O (O1, O2, O3, O4, O5) atoms. So in order to get a better picture of the motion of various polyhedral units (described below), the $\langle u^2 \rangle$ of polyhedral units around Y atoms are plotted separately. At 15 GPa, the structure of monoclinic phase consists of $YO_7$ polyhedra around Y1 (2O1, 3O3, 2O4) and Y2 (2O1, 3O2, O3, O5), while $YO_6$ polyhedra is formed around Y3 (O1, O2, 2O4, 2O5). At 48 GPa, Y3 atoms also form $YO_7$ (Y3, O1, O2, O3, 2O4, 2O5). The hexagonal phase also has seven coordinated polyhedral units around Y atoms (Y, 3O1, 4O2).

translational motions of all the atoms. At higher energies (above 35 meV), the O atoms have large amplitude vibrations compared to the Y atoms, thus involving Y-O stretching and rotational motion of the $YO_6$ units.

At 15 GPa, the structure of the monoclinic phase consists of $YO_7$ and $YO_6$ polyhedra. The atoms connected to the various polyhedral units are labeled, as shown in Fig. 1. We find that for modes up to 5 meV, all the atoms have nearly the same amplitude, indicating a translational motion of the polyhedral units. Above 35 meV there is very low contribution from the Y atoms as compared to O atoms. However, there is substantial difference in the amplitude of various O atoms connected to Y, implying rotational motions along with the distortion of the polyhedral units.

Our free-energy calculations show that the monoclinic to hexagonal-phase transition occurs at 48 GPa. The calculated structure (Fig. 1) at 48 GPa shows that the coordination of the polyhedra formed around the Y3 atoms has changed. We find that the bond length of 3.05 Å at 15 GPa between the Y3 and O3 atoms has reduced to 2.68 Å at 48 GPa, which becomes comparable to other Y3-O (O1, O2, O4, and O5) bonds and thus results in an increase in the coordination number of Y3 from 6 to 7. Thus, we find that at 48 GPa all the Y (Y1, Y2, and Y3) atoms form $YO_7$ polyhedral. With increase in pressure the phonon modes have also shifted to higher energies. As explained previously, the shortening of the Y3-O3 distance is due to the movement of the O3 atom. This is also reflected in the $\langle u^2 \rangle$ plot, where we find that the contribution to $\langle u^2 \rangle$ from the phonon modes of the O3 atoms in the 30 to 40 meV range has large amplitude at this pressure as compared to that at 15 GPa. As expected for increasing pressure, the contribution to $\langle u^2 \rangle$ arises from modes at higher energies compared to those at 15 GPa.

In the hexagonal phase at 48 GPa, we find that the structure consists of $YO_7$ (consisting of 3O1 and 4O2), $O2Y_4$, and $O1Y_6$ polyhedral units. The calculated $\langle u^2 \rangle$ of the various atoms in the hexagonal phase at 48 GPa is shown in Fig. 12. We find that for modes up to about 40 meV the amplitudes of all the atoms are comparable, indicating the translational motion of $O1Y_6$ and $O2Y_5$. At energies above 50 meV, the oxygen atoms have significantly larger amplitude compared to that of the Y atoms. However, various O1 and O2 constituting the $YO_7$ have different $\langle u^2 \rangle$. This indicates rotational motion of $YO_7$ along with the distortion of the polyhedral units.

## VI. CONCLUSIONS

We have reported inelastic neutron scattering measurements on polycrystalline samples of $Y_2O_3$ in the cubic phase. The measurements are in agreement with *ab initio* as well as shell-model calculations. The calculated thermodynamic properties in the cubic phase also agree very well with the available experimental data. The free-energy calculations in various phases of $Y_2O_3$ help us to study the high-pressure phase transition behaviour of $Y_2O_3$. We have shown that the large compression of one of the Y-O bonds with increasing pressure in the monoclinic phase is responsible for the change of coordination around the Y atoms in the monoclinic phase. The transition from monoclinic to the hexagonal phase is found to be displacive in nature.

*Corresponding author: rmittal@barc.gov.in

[1]H. G. Scott, J. Mat. Sci. **10**, 1527 (1975).
[2]M. O. Marlowe and D. R. Wilder, J. Am. Ceram. Soc. **48**, 227 (1965).
[3]D. Schubert, R. Dargusch, J. Raitano, and S.-W. Chan, BBRC **342**, 86 (2006).
[4]G. Schaack and J. A. Koningstein, J. Optical Soc. Am **60**, 1110 (1970).
[5]V. M. Goldschmidt, F. Ulrich, and T. Barth, Skrifter Norske Vindenskaps-Akad. Oslo, I. Mat. Naturv. Kl. No. **5**, 5 (1925).
[6]M. G. Paton and E. N. Maslen, Acta Cryst. **19**, 307 (1965).
[7]B. H. O'Connor and T. M. Valentine, Acta Cryst. B **25**, 2140 (1969).
[8]H. R. Hoekstra and K. A. Gingerich, Science **146**, 1163 (1964).
[9]H. R. Hoekstra, Inorg. Chem. **5**, 754 (1966).
[10]V. Srikanth, A. Sato, J. Yoshimoto, J. H. Kim, and T. Ikegami, Cryst. Res. Technol. **29**, 981 (1994).
[11]E. Husson, C. Proust, P. Gillet, and J. P. Itie, Mat. Res. Bull. **34**, 2085 (1999).
[12]H. Yusa, T. Tsuchiya, N. Sata, and Y. Ohishiz, Inorg. Chem. **49**, 4478 (2010).
[13]L. Wang, Y. Pan, Y. Ding, W. Yang, W. L. Mao, S. V. Sinogeikin, Y. Meng, G. Shen, and H. Mao, Appl. Phy. Lett. **94**, 061921 (2009).
[14]T. Atou, K. Kusaba, K. Fukuoka, M. KiKuchi, and Y. Syono, J. Solid State Chem. **89**, 378 (1990).
[15]J. W. Palko, W. M. Kriven, S. V. Sinogeikin, J. D. Bass, and A. Sayir, J. Appl. Phy. **89**, 7791 (2001).
[16]V. Swamy, N. A. Dubrovinskaya, and L. S. Dubrovinsky, J. Mater. Res. **14**, 456 (1999).
[17]L. J. Alvarez, M. A. S. Miguel, and J. A. Odriozola, Phys. Rev. B **59**, 11303 (1999).
[18]A. B. Belonoshko, G. Gutierrez, R. Ahuja, and B. Johansson, Phys. Rev. B **64**, 184103 (2001).
[19]Y. Repelin, C. Proust, E. Husson, and J. M. Beny, J. Solid State Chem. **118**, 163 (1995).
[20]C. Bousige, S. Rols, J. Cambedouzou, B. Verberck, S. Pekker, É. Kováts, G. Durkó, I. Jalsovsky, É. Pellegrini, and P. Launois, Phys. Rev. B **82**, 195413 (2010).
[21]V. F. Sears, Neutron News **3**, 29 (1992) [www.ncnr.nist.gov]; A.-J. Dianoux and G. Lander, editors, *Neutron Data Booklet*, Institut Laue-Langevin, Grenoble, France (2002).
[22]J. P. Perdew, K. Burke, and M. Ernzerhof, Phys. Rev. Lett. **77**, 3865 (1996).
[23]H. J. Monkhorst and J. D. Pack, Phys. Rev. B **13**, 5188 (1976).
[24]P. Giannozzi, S. Baroni, N. Bonini, M. Calandra, R. Car, C. Cavazzoni, D. Ceresoli, G. L Chiarotti, M. Cococcioni, I. Dabo, A. D. Corso, S. de Gironcoli, S. Fabris, G. Fratesi, R. Gebauer, U. Gerstmann, C. Gougoussis, A. Kokalj, M. Lazzeri, L. Martin-Samos, N. Marzari, F. Mauri, R. Mazzarello, S. Paolini, A. Pasquarello, L. Paulatto, C. Sbraccia, S. Scandolo, G. Sclauzero,

A. P Seitsonen, A. Smogunov, P. Umari, and R. M Wentzcovitch, J. Phys. Condens. Matter **21**, 395502 (2009).

[25]S. L. Chaplot, N. Choudhury, S. Ghose, M. N. Rao, R. Mittal, and K. N. Prabhatasree, European Journal of Mineralogy **14**, 291 (2002).

[26]R. Mittal, S. L. Chaplot, and N. Choudhury, Progress of Materials Science **51**, 211 (2006).

[27]G. Venkatraman, L. Feldkamp, and V. C. Sahni, *Dynamics of Perfect Crystals* (MIT, Cambridge, 1975).

[28]P. Bruesch, *Phonons: Theory and Experiment* (Springer, Berlin, 1982) Vols. 1/2.

[29]S. L. Chaplot (Unpublished).

[30]M. Foex and J. P. Travese, Rev. Int. Hautes Temp. Refract. **3**, 429 (1966).

[31]J. X. Boucherle, Acta Cryst. B **31**, 2745 (1975).

[32]K. S. Gavrichev, V. E. Gorbunov, L. N. Golushina, G. E. Nikiforova, G. A. Totrova, and I. S. Shaplygin, Russ. J. Phys. Chem. **67**, 1554 (1993).

[33]T. S. Yashvili, D. S. Tsagareishvili, and G. G. Gvelesiani, Izv. Akad. Nauk GrSSR **46**, 409 (1967).

[34]U. Kolitsh, Hochtemperaturkalorimetrie und phasenanalytik in $SE_2O_3$-$Al_2O_3$-$SiO_2$ systemen, PhD dissertation, University of Stuttgart, 1995.

[35]Y. A. Landa, Y. A. Polonskii, B. S. Glazachev, and T. V. Milovidova, Refractories **2**, 86 (1974).

[36]JANAF Thermochemical Tables. J. Phys. Chem. Ref. Data, 3rd edition, **14**, (1985).

[37]T. Yamada, M. Yoshimura, and S. Somiya, High Temp. High Press. **18**, 377 (1986).

[38]A. Sjolander, Arkiv fur Fysik **14**, 315 (1958).